


# Contributions of the individual domains of $\alpha_{IIb}\beta_3$ integrin to its extension: Insights from multiscale modeling

Onkar Joshi<sup>1,2</sup> | Tomasz Skóra<sup>2</sup> | Anna Yarema<sup>1</sup> | Richard D. Rabbitt<sup>1</sup> | Tamara C. Bidone<sup>1,2,3,4</sup> 

<sup>1</sup>Department of Biomedical Engineering, University of Utah, Salt Lake City, Utah, USA

<sup>2</sup>Scientific Computing and Imaging Institute, University of Utah, Salt Lake City, Utah, USA

<sup>3</sup>Department of Molecular Pharmaceutics, University of Utah, Salt Lake City, Utah, USA

<sup>4</sup>Department of Biochemistry, University of Utah, Salt Lake City, Utah, USA

## Correspondence

Tamara C. Bidone, Department of Biomedical Engineering, University of Utah, Salt Lake City, UT 84112, USA.

Email: [tamarabidone@sci.utah.edu](mailto:tamarabidone@sci.utah.edu)

## Funding information

National Institutes of Health, Grant/Award Number: 1R35GM147491-01

## Abstract

The platelet integrin  $\alpha_{IIb}\beta_3$  undergoes long-range conformational transitions between bent and extended conformations to regulate platelet aggregation during hemostasis and thrombosis. However, how exactly  $\alpha_{IIb}\beta_3$  transitions between conformations remains largely elusive. Here, we studied how transitions across bent and extended-closed conformations of  $\alpha_{IIb}\beta_3$  integrin are regulated by effective interactions between its functional domains. We first carried out  $\mu$ s-long equilibrium molecular dynamics (MD) simulations of full-length  $\alpha_{IIb}\beta_3$  integrins in bent and intermediate conformations, the latter characterized by an extended headpiece and closed legs. Then, we built heterogeneous elastic network models, perturbed inter-domain interactions, and evaluated their relative contributions to the energy barriers between conformations. Results showed that integrin extension emerges from: (i) changes in interfaces between functional domains; (ii) allosteric coupling of the head and upper leg domains with flexible lower leg domains. Collectively, these results provide new insights into integrin conformational activation based on short- and long-range interactions between its functional domains and highlight the importance of the lower legs in the regulation of integrin allostery.

## KEYWORDS

heterogeneous elastic network modeling, integrin extension, molecular dynamics, multiscale modeling

## 1 | INTRODUCTION

Integrins are transmembrane heterodimeric receptors that mediate cell adhesions to the extracellular matrix or other cells by transmitting bidirectional signals and mechanical force (Bouvard et al., 2013; Campbell & Humphries, 2011; Chen, 2008; Hynes, 2002; Paszek & Weaver, 2004; Puklin-Faucher & Sheetz, 2009; Puklin-Faucher &

Vogel, 2009).  $\alpha_{IIb}\beta_3$  integrin is highly expressed on the surface of platelets and plays a critical role in hemostasis and thrombosis (Bennett et al., 2009; Botero, 2020; Chen et al., 2019; Jackson, 2011; Kröll et al., 1996; Li et al., 2010; Ma et al., 2007; Nesbitt et al., 2002, 2009; Shen et al., 2013; Stalker et al., 2013; Tello-Montoliu et al., 2012). Like other integrins,  $\alpha_{IIb}\beta_3$  exists in a dynamic equilibrium between bent and extended conformations, corresponding to transitions between inactive and active states with different affinities for binding extracellular ligands (Bennett, 2005; Bennett et al., 2009; Li et al., 2010;

Onkar Joshi and Tomasz Skóra contributed equally to the project as the co-first authors.

This is an open access article under the terms of the [Creative Commons Attribution-NonCommercial-NoDerivs](https://creativecommons.org/licenses/by-nc-nd/4.0/) License, which permits use and distribution in any medium, provided the original work is properly cited, the use is non-commercial and no modifications or adaptations are made.

© 2024 The Authors. *Cytoskeleton* published by Wiley Periodicals LLC.

Moore et al., 2018; Parise, 1999; Payrastra et al., 2000; Shattil et al., 1998; Shen et al., 2013; Stalker et al., 2013).

Integrin conformational activation occurs through extension of the extracellular region (Figure 1a), also known as the ectodomain, and separation of the transmembrane helices (Chen et al., 2023; Hanein & Volkman, 2018). The ectodomain of  $\alpha_{IIb}\beta_3$  integrin comprises several functional domains (Figure 1a) that interact with one another at short and long distances. The  $\alpha$  subunit contains an N-terminal seven-bladed  $\beta$ -propeller domain, forming the  $\alpha$  part of the head (Figure 1b), followed by the Thigh domain, and two calf domains, forming the  $\alpha$  part of the legs (Figure 1b). The  $\beta$  subunit consists of an N-terminal  $\beta$ -I domain, forming the  $\beta$  part of the head (Figure 1b), followed by the Hybrid domain, the plexin-semaphorin-integrin domain (PSI), four cysteine-rich epidermal growth factor (EGF) modules (I-EGF) 1-4, and  $\beta$ -T domains, collectively forming the  $\beta$  part of the legs (Figure 1b). Ectodomain head and legs connect to membrane spanning helices ending with C-terminal cytoplasmic tails that connect to the cell cytoskeleton (Figure 1a). In the bent conformation, head and upper legs, forming the head region or headpiece ( $\beta$ -propeller and Thigh domains from  $\alpha$  subunit and  $\beta$ -I, Hybrid, and PSI domains from the  $\beta$  subunit, see Figure 1b), are bent toward the membrane and form an extensive interface with domains of the lower legs (Calf and EGF domains). Disruption of this interface promotes flattening of the  $\alpha$  and  $\beta$  knees, positioned between Thigh/Calf-1 and between EGF-1/EGF-

2. Conformations with an extended headpiece and closed legs (Figure 1a) have been identified as integrin intermediates (Chen et al., 2019; Nishida et al., 2006; Takagi et al., 2002; Xu et al., 2016; Xin, 2023).

High-resolution reconstructions of  $\alpha_{IIb}\beta_3$  integrin have suggested that the extension of integrin occurs through rigid body-based motions, in which the functional domains move as rigid units with joints between them (Adair & Yeager, 2002). These joints correspond to several linker regions: at the interfaces between  $\beta$ -propeller/Thigh, Thigh/Calf-1, EGF-1/EGF-2, and Hybrid/EGF-1, indicated by green arrows in Figure 1b (Campbell & Humphries, 2011; Kolasangiani et al., 2022).

Ligand binding, divalent cations, and mechanical force allosterically link the ligand binding site, between  $\beta$ -propeller/ $\beta$ -I domains, with the distal end of the  $\beta$ -I domain, at the interface with the Hybrid domain to promote  $\beta$ -I/Hybrid hinge opening (Xiong, 2001; Adair & Yeager, 2002; Barton et al., 2004; Friedland et al., 2009; Kamata et al., 2010; Kong et al., 2009; Luo et al., 2003; Mould et al., 1995, 2003; Puklin-Faucher & Sheetz, 2009; Puklin-Faucher & Vogel, 2009; Takagi et al., 2002, 2003). These motions are transmitted to the  $\beta$  leg domains through the PSI domain (Xiao et al., 2004; Jallu, 2012). Interestingly, the PSI domain exhibits inherent flexibility, like the EGF domains which contain many disordered regions, and often these parts of integrin are not visible in cryo-EM maps (Schumacher

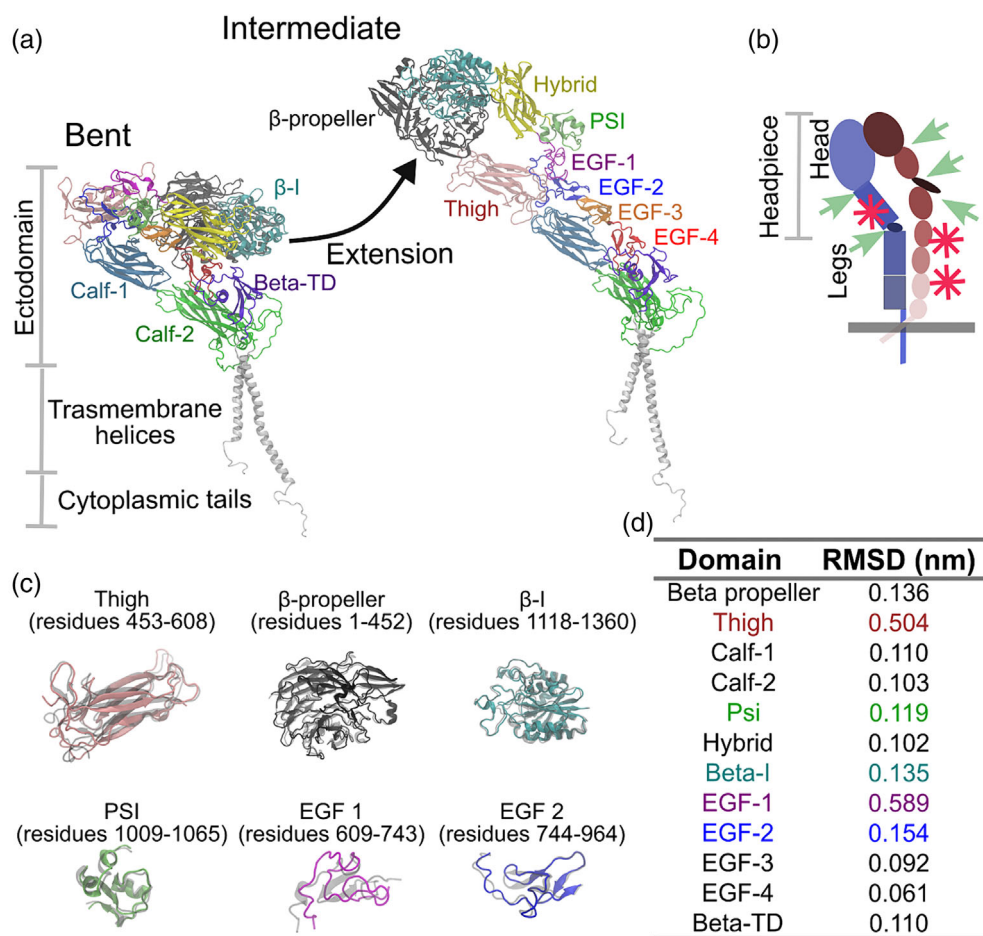


**FIGURE 1** Representation of bent and intermediate  $\alpha_{IIb}\beta_3$  integrin. (a) Secondary structure representation of bent and intermediate integrins, with the extracellular domains indicated in different colors. (b) Schematic representation of the functional domains of integrin. The head includes the  $\alpha$  subunit  $\beta$ -propeller and the  $\beta$  subunit  $\beta$ -I domains. The leg domains include the  $\alpha$  subunit Thigh, and Calf domains, and the  $\beta$  subunit Hybrid, PSI, EGF, and  $\beta$ -TD domains. The headpiece is formed by the head ( $\beta$ -propeller and  $\beta$ -I) and upper leg domains (Thigh, Hybrid, PSI, and EGF-1). Green arrows indicate flexible interdomain joints. The red asterisks indicate flexible domains. (c) Superposition of bent (gray) and intermediate (color) domains that present the largest differences between bent and intermediate  $\alpha_{IIb}\beta_3$  integrin. (d) Values of root mean square displacements between extracellular domains of  $\alpha_{IIb}\beta_3$  integrin in bent and intermediate conformations.

et al., 2021). The flexibility of the  $\beta$  subunit leg domains PSI and EGF (red asterisks in Figure 1b) could be capable of governing allostery, but the mechanisms remain unclear (Hilser & Thompson, 2007; Smaghe et al., 2010; Motlagh, 2014; Zhou, 2018).

With no currently existing experimental methods to gain dynamic insights into how the domains of integrin contribute to conformational activation, here we used multiscale modeling. We first carried out several  $\mu\text{s}$ -long equilibrium molecular dynamics (MD) simulations of full-length  $\alpha_{\text{IIb}}\beta_3$  integrin in bent and intermediate conformations, followed by other  $\mu\text{s}$ -long MD simulations of each extracellular domain separately. Then, we built heterogeneous elastic network models (hENMs) of bent and intermediate integrins, and systematically varied the effective interaction between domains, to bias the bent conformation toward the intermediate, and assessed the contributions of interdomain interactions to integrin extension. Our results demonstrate that specific interfaces of the head and upper leg domains provide short-range coupling for transmission of motion, whereas long-range interactions of these domains with the flexible lower leg domains contribute to the energy barriers between conformations. Disturbing these interactions in cells by ligand, cation binding, mechanical force, or combinations of them, can facilitate integrin extension and platelet activation.

## 2 | RESULTS

### 2.1 | Comparison of extracellular domains of $\alpha_{\text{IIb}}\beta_3$ integrins from cryo-EM

We first evaluated structural differences between domains of bent and intermediate  $\alpha_{\text{IIb}}\beta_3$  integrins. We extracted the domains from the cryogenic electron microscopy (cryo-EM) reconstructions of full-length integrins, which were previously extracted from human platelets and embedded in lipid nanodiscs (Xu et al., 2016). The domains were cropped from the bent full-length conformer and structurally aligned based on the Kabsch method in VMD (Humphrey et al., 1996; Kabsch, 1978). This method computes the transformation needed to move one domain (from bent integrin) onto another (from intermediate integrin) by minimizing the root mean square displacements (RMSD) of corresponding alpha carbons,  $C_\alpha$  (aligned structures of representative domains are reported in Figure 1c). Then, after the alignment, the  $C_\alpha$  RMSD of each domain pair was assessed (Figure 1d). Thigh and EGF-1 domains presented the highest  $C_\alpha$  RMSD (values  $>0.5$  nm). EGF-2 presented  $C_\alpha$  RMSD  $\sim 0.15$  nm (Figure 1d).  $\beta$ -propeller and  $\beta$ -I domains presented comparable  $C_\alpha$  RMSD, of  $\sim 0.135$  nm. PSI, Calf-1,  $\beta$ -TD presented  $C_\alpha$  RMSD around 0.11 nm, and the remaining domains presented  $C_\alpha$  RMSD around or below 0.1 nm (Figure 1d). In sum, the  $\alpha$ -subunit Thigh domain and the  $\beta$ -subunit EGF-1 and EGF-2 domains, forming the knees of integrin, presented the highest structural differences between bent and intermediate conformations, followed by  $\beta$ -propeller and  $\beta$ -I domains, which form the ligand binding site. Higher values of  $C_\alpha$  RMSD for the headpiece and upper leg domains relative to the lower leg domains suggest that the

major structural changes during conformational activation occur in the head, knees, and upper legs.

### 2.2 | Analysis of MD trajectories of bent and intermediate $\alpha_{\text{IIb}}\beta_3$

To evaluate the molecular dynamic properties of the extracellular domains of  $\alpha_{\text{IIb}}\beta_3$  integrins, we carried out 4.5  $\mu\text{s}$  of equilibrium MD simulations on the bent and intermediate conformations (Xu et al., 2016), embedded in lipid bilayers (Figure 2a). At the end of the simulations,  $C_\alpha$  RMSD with respect to the input configuration was

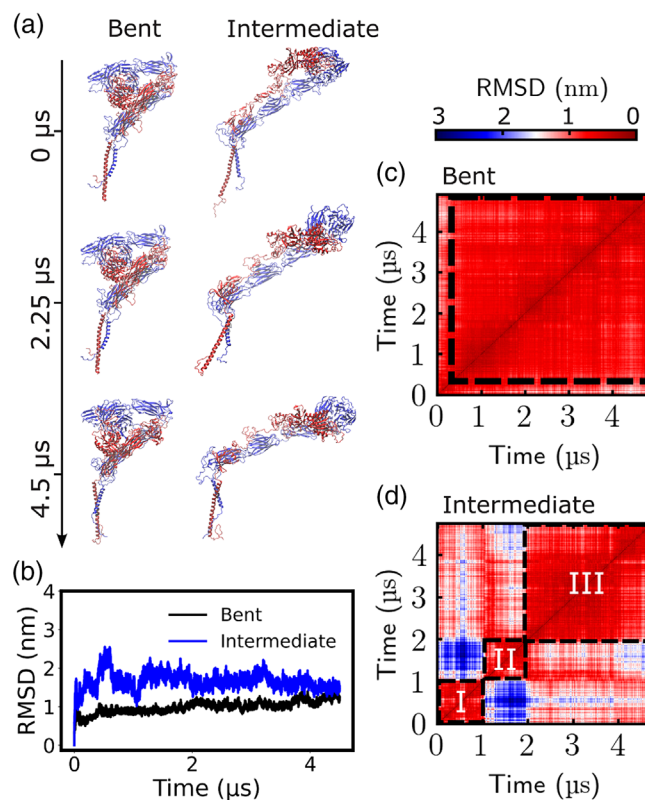


**FIGURE 2** Evaluation of structural stability of bent and intermediate  $\alpha_{\text{IIb}}\beta_3$  integrin. (a) Snapshots of bent and intermediate  $\alpha_{\text{IIb}}\beta_3$  integrins at the onset of equilibrium molecular dynamics (MD) simulations, at 2.25 and at 4.5  $\mu\text{s}$ . New cartoon representation of the all-atom models with  $\alpha$  subunit in blue and  $\beta$  subunit in red. (b) Root mean square displacements (RMSD) values for  $C_\alpha$  atoms of bent and intermediate  $\alpha_{\text{IIb}}\beta_3$  integrins calculated with respect to the corresponding initial, energy minimized and equilibrated states, throughout 4.5  $\mu\text{s}$  of equilibrium MD simulations. (c) Pairwise  $C_\alpha$  RMSD of bent  $\alpha_{\text{IIb}}\beta_3$  integrin throughout 4.5  $\mu\text{s}$  of equilibrium MD simulations. The red color represents an RMSD  $<1$  nm between consecutive structures and indicates that one conformational state is sampled. (d) Pairwise  $C_\alpha$  RMSD of intermediate  $\alpha_{\text{IIb}}\beta_3$  integrin throughout 4.5  $\mu\text{s}$  of equilibrium MD simulations. The first state with RMSD  $<1$  nm emerges within 1  $\mu\text{s}$  (square area for state I). The second state with RMSD  $<1$  nm emerges between 1 and 2  $\mu\text{s}$  (square area for state II). The third and final state with RMSD  $<1$  nm emerges between 2 and 4.5  $\mu\text{s}$  (square area for state III).

1.20 nm for bent integrin and 1.49 nm for the intermediate (Figure 2b). The intermediate conformation presented peaks in  $C_{\alpha}$  RMSD of >2 nm mostly below 1  $\mu$ s and it stabilized between 1 and 1.5 nm above 1  $\mu$ s (Figure 2b). To evaluate the  $C_{\alpha}$  RMSD of each frame in the trajectory relative to all other frames, pairwise  $C_{\alpha}$  RMSD was also computed. For bent integrin, conformational convergence started from a few hundreds of ns (Figure 2c), with an average  $C_{\alpha}$  RMSD of  $\sim$ 0.5 nm. For intermediate integrin, conformational convergence started from  $\sim$ 2  $\mu$ s (Figure 2d), with average  $C_{\alpha}$  RMSD of  $\sim$ 0.7 nm. Between 0 and 2  $\mu$ s of MD simulations, the intermediate conformation transitioned across two other states with  $C_{\alpha}$  RMSD <1 nm: the first state occurred between 0 and 1  $\mu$ s; and the second state occurred between 1 and 2  $\mu$ s (Figure 2d). Therefore, structural changes in the intermediate conformation occurred throughout the simulations, but for more than half the simulation time, both bent and intermediate integrins maintained a relatively stable conformation (Figure 2b-d).

Collectively, results from analysis of  $C_{\alpha}$  RMSD of bent and intermediate  $\alpha_{IIb}\beta_3$  integrins during equilibrium MD simulations indicated that bent integrin is more stable than the intermediate, consistent with previous equilibrium MD studies of the same conformations (Dasetty et al., 2023; Tong et al., 2023).

### 2.3 | MD properties of extracellular domains of $\alpha_{IIb}\beta_3$

To evaluate how the extracellular domains control conformational transitions of integrin, we analyzed  $C_{\alpha}$  RMSD and root mean square fluctuation (RMSF) of each domain within the full-length integrins and compared these quantities with those from the same domains in isolation. Then, we evaluated the buried solvent-accessible surface area (SASA), of several domain pairs within bent and intermediate integrins.

The overall  $C_{\alpha}$  RMSFs of the two full-length integrins presented values between 0.03 and 1.19 nm with averages  $\sim$ 0.15 nm (Figure 3a). The average  $C_{\alpha}$  RMSD of the functional domains, computed between 2 and 4  $\mu$ s of simulations, was lower when the domains were embedded within integrin (between 0.1 and 0.7 nm) than in isolation (between 0.1 and 1.3 nm) because of stabilizing interactions with other domains (Figure 3b, top). The average  $C_{\alpha}$  RMSD of the domains within full-length integrins presented the highest values for the  $\beta$  subunit EGF domains (Figure 3b, top). In the  $\beta$  subunit, EGF-1 from the bent conformation showed  $\sim$ 8% higher RMSD with respect to the intermediate, whereas EGF-2, EGF-3, and EGF-4 presented up to  $\sim$ 3-fold higher RMSD for the intermediate conformation with respect to the bent (Figure 3b, top). All domains in the  $\alpha$ -subunit presented significant differences in average RMSD between bent and intermediate conformations. The thigh domain presented higher average  $C_{\alpha}$  RMSD in the intermediate conformation ( $\sim$ 0.4 vs. 0.35 nm), and Calf-1 domain presented higher  $C_{\alpha}$  RMSD in the bent ( $\sim$ 0.2 vs.  $\sim$ 0.1 nm; Figure 3b, top).  $C_{\alpha}$  RMSD over time for the different domains are reported in Figures S1 and S2. EGF1-4 showed the

highest RMSD both within full-length integrins and when isolated, followed by Calf-2, and  $\beta$ -TD (Figure 3b, top and Figures S1 and S2).

$C_{\alpha}$  RMSF of the extracellular domains were between 0.08 and 0.5 nm for the two full-length integrins, and between 0.08 and 0.8 nm for the isolated domains (Figure 3b, bottom). The highest  $C_{\alpha}$  RMSF were observed for isolated PSI, EGF1-4, Calf-2, and  $\beta$ -TD (Figure 3b, bottom). When embedded within the protein, EGF1-4 presented the highest fluctuations relative to other domains, with values between 0.15 and 0.5 nm (Figure 3b, bottom), again showing the high dynamics of the lower leg domains of integrin. Alike the  $C_{\alpha}$  RMSD,  $C_{\alpha}$  RMSF were  $\sim$ 10% higher for EGF-1 in the bent conformation with respect to the intermediate, and up to 2-fold higher for EGF-2, EGF-3, and EGF-4 in the intermediate with respect to bent (Figure 3b, bottom). Similar to the  $C_{\alpha}$  RMSDs, the  $\alpha$ -subunit domains presented slightly higher or comparable  $C_{\alpha}$  RMSFs in isolation in relation to the same domains while within the protein.  $C_{\alpha}$  RMSFs of each residue of the different domains are reported in Figure S3. Residues of the four EGF domains had significantly higher  $C_{\alpha}$  RMSFs in isolation versus within the protein. These domains also had enhanced deviations from their average  $C_{\alpha}$  radius of gyration ( $R_g$ ) when in isolation (Figure S5), indicating intrinsic flexibility.

The SASA that is buried between pairs of neighbor extracellular domains was calculated as summing over the SASA of the two domains separately minus the SASA of the laterally paired domains, divided by two, given as:

$$\text{buried SASA} = \frac{1}{2} \{ [\text{SASA}(\text{domain1}) + \text{SASA}(\text{domain2})] - \text{SASA}(\text{paired domains}) \} \quad (1)$$

The buried SASA for bent and intermediate conformations presented average values of up to  $\sim$ 18 nm<sup>2</sup> (Figure 3c). Consistent with expectations, as the SASA of integrin increases from bent to intermediate (Kolasangiani et al., 2022), their buried SASA decreases (Figure 3c). The average buried SASA between the  $\beta$ -I/ $\beta$ -propeller domains, forming the ligand binding site, and between PSI/EGF-1, connecting the headpiece to the  $\beta$  subunit knee, significantly decreased from bent to intermediate (Figure 3c). Therefore, the identified decrease in buried SASA from our simulations can be related to the opening of the ligand binding site from bent to intermediate states of integrin, and to a reduced coupling of the PSI domain to the EGF-1 in the intermediate versus bent conformations. Additionally, in the bent conformation, the Hybrid domain forms interfaces with  $\beta$ -TD and EGF3-4 domains, with average buried SASA between 1 and 4.6 nm<sup>2</sup>, but these interfaces disappear in the intermediate conformation (Figure 3c). The buried SASA between Thigh/Calf-1 and EGF-2/EGF-3 increased from bent to intermediate (Figure 3c), which can be related to knees flattening upon activation and headpiece extension, respectively (Puklin-Faucher & Sheetz, 2009; Puklin-Faucher & Vogel, 2009; Springer et al., 2008; Takagi et al., 2002; Xiao et al., 2004).

In sum, analysis of  $C_{\alpha}$  RMSD and RMSF indicated that the lower  $\beta$  leg domains are flexible. Evaluation of buried SASA demonstrated that



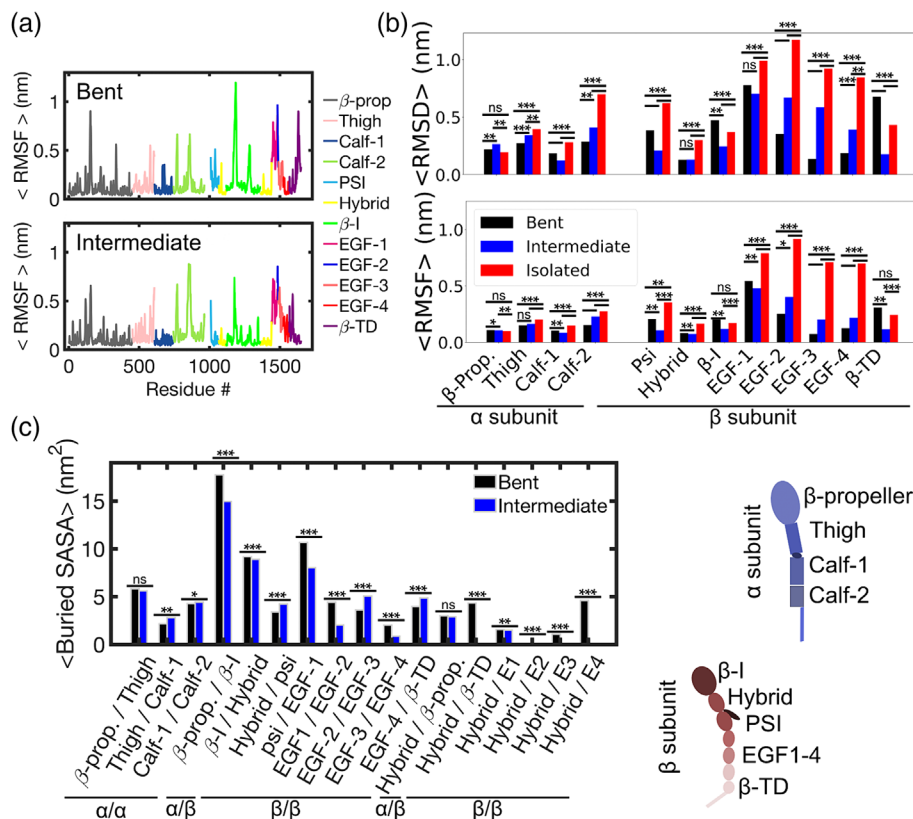


**FIGURE 3** Evaluation of structural stability of the extracellular domains of bent and intermediate  $\alpha_{11b}\beta_3$  integrin. (a) Average root mean square fluctuation (RMSF) for  $C_\alpha$  atoms of bent and intermediate  $\alpha_{11b}\beta_3$  integrins. Extracellular domains are in different colors. (b) Average root mean square displacement (RMSD) values for  $C_\alpha$  atoms of each extracellular domain of integrin when embedded within bent and intermediate conformations and when in isolation (upper panel). Min and max standard errors of the mean RMSD for bent and intermediate are 0.0006 and 0.05 nm and 0.001 and 0.06 nm, respectively. For isolated domains, minimum and maximum standard errors of the mean RMSD are 0.001 and 0.01 nm, respectively. Average RMSF values for  $C_\alpha$  atoms of each extracellular domain of integrin when embedded within bent and intermediate conformations and when in isolation (lower panel). Min and max standard errors of the mean RMSF of bent and intermediate conformations are 0.001 and 0.02 nm, and 0.001 and 0.03 nm, respectively. For isolated domains, minimum and maximum errors of the mean RMSF are 0.002 and 0.09 nm, respectively. (c) Average buried SASA for different pairs of extracellular domains of integrin in bent and intermediate conformations. Error bars indicate standard deviations of the mean. Standard errors of the mean are between 0 and 0.4 nm<sup>2</sup>. For the full-length integrins, average RMSD, RMSF, and buried SASA are calculated between 2 and 4.5  $\mu$ s of equilibrium molecular dynamics (MD) simulation; for the isolated domains, the average RMSD, RMSF, and buried SASA are calculated as the mean of three independent equilibrium MD replicas of 1  $\mu$ s each. \* $p < 0.1$ , \*\* $p < 0.05$ , \*\*\* $p < 0.001$  from two-sample t-test.

molecular interfaces corresponding to flexible interdomain joints (green arrows in Figure 1b) either decreased ( $\beta$ -I/ $\beta$ -propeller, and PSI/EGF-1) or increased (Thigh/Calf-1 and EGF-2/EGF-3) in the transition from bent to intermediate conformation.

## 2.4 | Comparative analysis of $\alpha_{11b}\beta_3$ hENMs of bent and intermediate integrin

To evaluate the effects of interdomain interactions on integrin extension, hENMs (Lyman et al., 2008) were built. Bent and intermediate integrin structures were first coarse-grained by reducing each functional domain into a bead corresponding to the center of geometry of its residues. The algorithm seeks the set of harmonic interaction potentials that minimize the difference between the MD and hENM normal mode bead fluctuations. CG representations of bent and

intermediate integrins are shown overlaid on the corresponding groups of  $C_\alpha$  in Figure 4a.

The effective force constants for bent hENM were broadly distributed, with a mean of 20.2 kcal/mol/nm<sup>2</sup> and a standard deviation of 40.3 kcal/mol/nm<sup>2</sup> (Figure 4b). Compared with that, the intermediate hENM exhibited lower mean, of 14.4 kcal/mol/nm<sup>2</sup> and similar standard deviation of 43.6 kcal/mol/nm<sup>2</sup> (Figure 4b). In agreement with higher, on average, values of force constants, the mean equilibrium distances between domain pairs were smaller for bent hENM: 6.5 nm (standard deviation of 3.4 nm), than for the intermediate hENM: 7.1 nm (standard deviation of 3.3 nm, like the value for the bent hENM).

For bent hENM, more than 80% of effective force constants were  $< 25$  kcal/mol/nm<sup>2</sup> (Figure 4c). Within the remaining 20% of interdomain interactions, the domain pairs with the highest effective force constants were: Hybrid/ $\beta$ I (121.8 kcal/mol/nm<sup>2</sup>), Hybrid/EGF-4

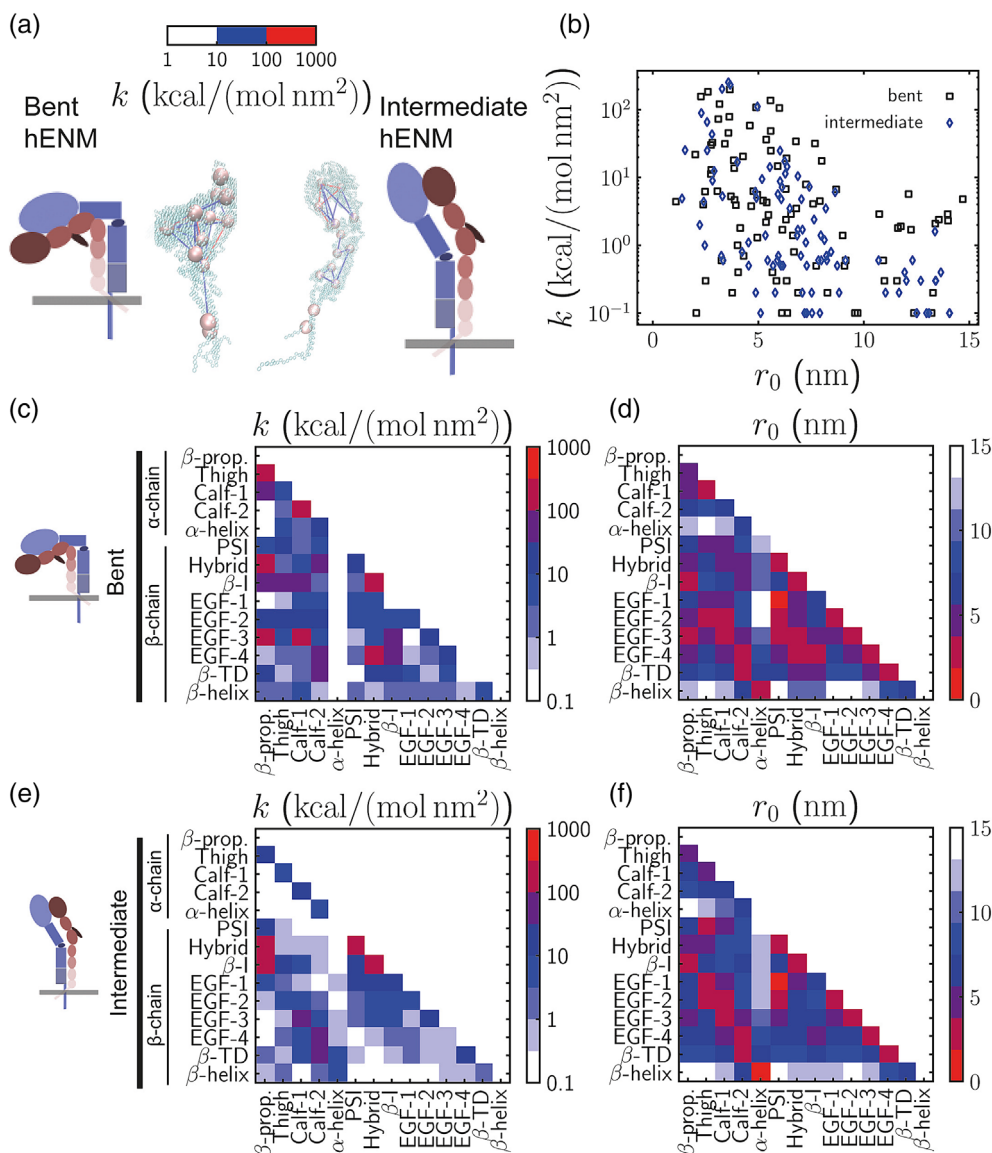


**FIGURE 4** Heterogeneous elastic network models (hENMs) of bent and intermediate integrin structures. (a) Representation of coarse-grained models of bent and intermediate integrin overlaid on smaller beads representing C $\alpha$ . The larger beads represent the centers of geometry of the C $\alpha$ 's of each domain. Links between the CG sites represent substantial domain–domain interactions from hENM, with colors representing the respective force constants. (b) Scatter plot of hENM force constant–equilibrium distance pairs for all 91 domain–domain pairs obtained in bent and intermediate states. (c) Force constants and (d) equilibrium distances in bent hENM represented by color-coded matrices. (e) Force constants and (f) equilibrium distances in intermediate hENM represented by color-coded matrices. Owing to the matrices' symmetry and diagonal elements being 0, on panels (c–f) only elements below the main diagonals are shown.

(183.9 kcal/mol/nm $^2$ ), Hybrid/ $\beta$ -propeller (108.2 kcal/mol/nm $^2$ ),  $\beta$ -propeller/Thigh (137.9 kcal/mol/nm $^2$ ),  $\beta$ -propeller/EGF-3 (199.1 kcal/mol/nm $^2$ ), Calf-1/Calf-2 (106.6 kcal/mol/nm $^2$ ), and Calf-1/EGF-3 (157.5 kcal/mol/nm $^2$ ) as shown in Figure 4c. The strongest effective interactions in bent hENM involved the Hybrid and  $\beta$ -propeller domains, suggesting strong coupling of these domains to others (Figure 4c).

For intermediate hENM, more than 80% of the effective force constants were below 9 kcal/mol/nm $^2$  (Figure 4e), a value significantly below most of the interactions in bent hENM. The maximum interaction constant for intermediate hENM was 254.6 kcal/mol/nm $^2$  for Hybrid/PSI, followed by 233.7 kcal/mol/nm $^2$  for  $\beta$ -propeller/ $\beta$ 1, 203.5 kcal/mol/nm $^2$  for Hybrid/ $\beta$ 1 (Figure 4e and Figure S6), and 111.6 kcal/mol/nm $^2$  for  $\beta$ -propeller/Hybrid. Although on average the interactions in intermediate hENM were weaker than in bent hENM, the strongest interactions in intermediate hENM present higher force constants than the strongest interactions in bent hENM. As expected, the Hybrid domain of the intermediate hENM presented an

equilibrium distance from Calf-1, Calf-2, EGF-3, EGF-4, and  $\beta$ -TD more than 2.5 nm larger than in the bent conformation (Figure 4d,f).

In sum, the mostly weaker effective interactions between domains in the intermediate conformation with respect to the bent conformation reflect a decrease in domain correlations from bent to intermediate. The substantial increase in equilibrium distances between the head and lower legs domains of integrin confirms the role of these domains in the slow structural dynamics of integrin extension (Gaillard et al., 2009; Puklin-Faucher et al., 2006).

## 2.5 | Brownian dynamics simulations of bent and intermediate hENMs

To evaluate the contribution of the extracellular domains of  $\alpha$ <sub>IIb</sub> $\beta$ <sub>3</sub> integrin to its extension, we ran 100  $\mu$ s of Brownian dynamics (BD) simulations of bent and intermediate hENMs. To track to what extent the structures in BD simulations resemble the intermediate

conformation, we computed the RMSD of these conformations over time, with respect to the intermediate BD structure averaged over the whole BD trajectory. Bent hENM presented an average RMSD of  $2.96 \pm 0.05$  nm (av. RMSF = 0.44 nm), whereas the intermediate hENM presented an average RMSD of  $0.9 \pm 0.3$  nm (av. RMSF = 0.9 nm; Figure 5a). Like the residue fluctuations of the all-atom intermediate conformation (Figure 2c), fluctuations in RMSD were higher for intermediate hENM than bent hENM, indicating lower structural stability of the former state (Figure 5a).

To evaluate how interdomain interactions affect the transition of integrin from bent to intermediate conformations, the effective interactions of the bent hENM were changed: first, the potential energy expression of the intermediate hENM was applied to the bent conformation (*swapped hENM*); second, the “stabilizing” interactions of bent hENM were removed, leaving the other interactions unaltered (*reduced hENM*); last, the potential energy expression for the intermediate hENM was used in the bent conformation and the stabilizing interactions were turned off (*both*).

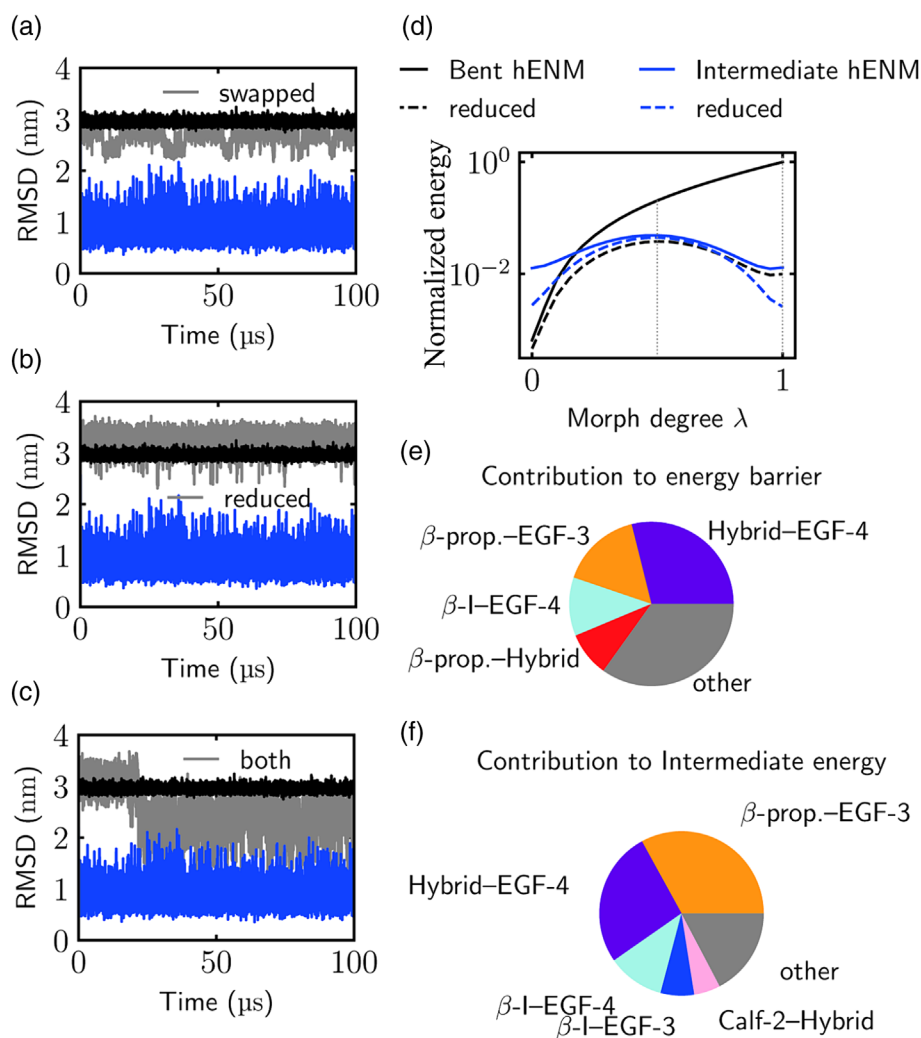


**FIGURE 5** Energy landscape of integrin is complex, and specific pairwise interactions between domains prevent relaxation to a thermodynamically favored state. (a) Changes in similarity to average intermediate heterogeneous elastic network models (hENM) structure quantified by root mean square displacements (RMSD) in time in Brownian dynamics (BD) simulations of coarse-grained integrin model governed by bent hENM (black), and intermediate hENM (blue). The gray curve denotes a system governed by intermediate hENM but starting from a bent initial configuration. RMSD is computed relative to the average intermediate structure from BD simulation. The gray curve does not relax to values of the blue one, but rather shifts down ca. 13%. (b) Gray curve denotes the simulation of reduced bent hENM, which is bent hENM without the terms corresponding to domains for which dimensionless displacement is larger than 3, which are deemed to destabilize the intermediate structure to the largest extent. Similarly to panel (a), the system does not relax to the intermediate structure. (c) Gray curve denotes the combination of the approaches introduced above, that is, swapping the intermediate hENM for bent hENM and turning off the terms with high dimensionless displacement. (d) Normalized potential energy computed from the hENM expressions along the coordinate of linear morphing between bent and intermediate structure (Video S1). Energy is plotted in log scale and normalized by the maximum. (e) Contributions of individual domain–domain interactions in bent hENM to the total potential energy in the middle point of linear morphing. Interactions between these domains stabilize bent state over the intermediate state kinetically, that is, slow down the transition. (f) Contributions of individual domain–domain interactions in bent hENM to the total potential energy of the intermediate structure—the end point of linear morphing. Interactions between these domains destabilize the intermediate state relative to the bent state thermodynamically.

Intuitively, one would expect a system governed by the intermediate hENM potential energy expression to evolve into the intermediate conformation. However, the RMSD from BD simulation of the *swapped* hENM was  $2.7 \pm 0.2$  nm (av. RMSF = 1.03 nm), only 13% lower than bent hENM, indicating that integrin became only slightly more akin to the intermediate hENM. The bent hENM did not relax completely into the intermediate conformation (Figure 5a), suggesting that some critical interactions from intermediate hENM prevent integrin extension.

In turn, the RMSD of the *reduced* hENM was  $3.3 \pm 0.2$  nm (av. RMSF = 1.07 nm), a value even higher than the average RMSD of bent hENM and also presenting higher fluctuations (Figure 5b). Finally, combining both approaches, that is, swapping the intermediate hENM into the bent conformation and reducing the hENM, significantly reduced the RMSD of bent hENM. Simultaneously swapping, and reducing the system, yielded, on average, 23.4% change in RMSD toward the intermediate conformation (Figure 5c). Notably, the time evolution exhibited a jump of ca. 0.78 nm after 22  $\mu$ s between states of RMSD 3.10 and 2.32 nm (Figure 5c). The stability of the bent conformation and the surprisingly small effects from hENM swapping and reduction suggest the existence of a complex conformational landscape with multiple energy barriers between bent and extended conformations.

## 2.6 | Evaluation of energy barriers for $\alpha_{IIb}\beta_3$ integrin extension

To gain insights into the energy landscape underlying integrin extension at the CG level, a sequence of conformations between bent and intermediate conformations was created using linear morphing. Evaluating the potential energy expression for bent hENM in each morphed conformation yielded a substantial increase in total energy with increasing  $\lambda$ , up to a maximum in the intermediate state of  $\sim 5700$  kcal/mol (black line in Figure 5d). 28.9% of energy at  $\lambda = 0.5$  was due to the effective interaction between Hybrid/EGF-4 domains, followed by 15.9% due to  $\beta$ -propeller/EGF-3, 11.5% due to  $\beta$ -I/EGF-4, and 8.8% due to  $\beta$ -propeller/Hybrid interactions (Figure 5e). Terms in interaction potential that prevented stabilization of the intermediate conformation ( $\lambda = 1$ ) were among:  $\beta$ -propeller/EGF-3 (33.0%), Hybrid/EGF-4 (26.7%),  $\beta$ -I/EGF-4 (11.2%), and  $\beta$ -I/EGF-3 (6.6%). An evaluation of the potential energy for bent hENM in the first and second intermediate states emerging from equilibrium MD simulations (between 0–1 and 1–2  $\mu$ s, see Figure 2d) is reported in Figure S7 and shows similar contributions from interactions among Hybrid,  $\beta$ -propeller, and EGF-3/4.

Consistent with the analysis of *swapped* RMSD yielding only 13% increase in similarity of the bent conformation with the intermediate one, incorporation of the intermediate hENM into the bent conformation lead to a new stable conformation akin to intermediate structure, but separated from the initial bent conformation by a large energy maximum of the order of 1500 kcal/mol (blue line in Figure 5d).

Using the *reduced* bent hENM led to an increase in total energy with increasing  $\lambda$  from bent to intermediate states up to values of the

order of 1000 kcal/mol in the middle ( $\lambda = 0.5$ ), followed by a decrease to a local minimum of the order of 300 kcal/mol (black-dashed lines in Figure 5d). The emergence of a local minimum in the intermediate conformation ( $\lambda \approx 1$ ) confirmed that dimensionless displacement (Equation 5) was an appropriate parameter to single out restraining interactions in the bent conformation but did not significantly decrease the magnitude of the energy barrier.

Using the *reduced* intermediate hENM led to an increase in total energy with decreasing  $\lambda$ , from intermediate to bent, up to a maximum ( $\sim 1200$  kcal/mol) in the middle ( $\lambda = 0.5$ ) followed by a decrease in energy to a level comparable to that of bent hENM (blue-dashed lines in Figure 5d).

In sum, results from conformational morphing and evaluation of the energy barriers across conformations suggest that during integrin extension, not only an energy barrier needs to be crossed, but also an energy minimum needs to emerge to stabilize the intermediate conformation. Both can be done by mostly weakening interactions of the head and Hybrid domains with the lower  $\beta$  leg domains (Figure 5e,f).

## 3 | CONCLUSIONS

The conformational dynamics of the platelet  $\alpha_{IIb}\beta_3$  integrin plays a pivotal role in the maintenance of the integrity of the vascular system and are implicated in platelet aggregation, thrombus formation, and bleeding disorders (Bennett, 2005; Bhatt & Topol, 2003; Shattil et al., 1985). However, how integrin transitions between bent and extended conformations remains largely elusive due to their timescale exceeding the capabilities of current all-atom MD simulations and the limitations of high-resolution experimental methods in capturing protein dynamics. Here, using equilibrium MD simulations and a coarse-grained approach involving hENMs, we show that: (i) changes of linker regions of headpiece domains underlie integrin extension; and (ii) most of the energy barrier for extension of bent integrin and stabilization of the intermediate originates from effective interactions between head and Hybrid domains with lower  $\beta$  leg domains (Figure 5e,f).

The importance of the lower leg domains for integrin conformational activation was recently demonstrated by structural studies based on cryo-EM (Huo et al., 2024), and our results are consistent with these findings. Analysis of the structural stability of membrane-embedded  $\alpha_{IIb}\beta_3$  conformations demonstrates that the bent state is more stable than the intermediate (Figure 2b,c). Accordingly, hENMs present stronger pairwise interactions between domains for the bent state (Figure 4b). As integrin transitions from bent to intermediate, several effective interactions need to be disrupted, specifically those between  $\beta$ -propeller, Hybrid, and  $\beta$ -I domains with EGF domains (Figure 4c and Figure 4e). Therefore, the enhanced fluctuations observed for the intermediate conformation with respect to bent integrin (Figure 3b), which correspond to weaker correlations between the motion of domains in hENM (Figure 4a,b), could originate from a loss of stabilizing long-range pairwise potentials with lower leg domains, as recently reported (Huo et al., 2024).



Regarding interdomain interactions at short scales, the interfaces between  $\beta$ -I/ $\beta$ -propeller and PSI/EGF-1 domains decrease from bent to intermediate (Figure 3c), indicating that the rearrangements of the ligand binding site are propagated to the legs through motions of the Hybrid domain (Puklin-Faucher & Sheetz, 2009; Puklin-Faucher & Vogel, 2009; Springer et al., 2008; Takagi et al., 2002; Xiao et al., 2004). Whereas the ligand binding site involves both  $\beta$ -propeller and  $\beta$ -I domains, the change in  $\beta$ -I plays a larger role for leg opening and transmits motion rigidly across the  $\beta$ -leg (Campbell & Humphries, 2011). Our results also showed that the PSI domain is flexible in solution and within bent integrin but not in intermediate (Figure 3b). In contrast, the EGF domains are highly flexible in solution and maintain some flexibility in both bent and intermediate integrins (Figure 3b), larger for EGF-1 and -2, smaller for EGF-3 and -4. It is conceivable that the flexibility of the PSI domain is not maintained in the more extended conformations as it transmits the motions of the headpiece to the lower legs (Campbell & Humphries, 2011; Xiao et al., 2004). In contrast, the flexibility of the lower EGF domains is maintained to ensure weakening of their interactions with the head domains, and therefore contribute to crossing the energy barrier between bent and extended conformation and stabilize integrin intermediate.

Linear morphing and evaluation of the potential energy at each stage of morphing indicated that the major contributors to the energy barrier separating bent and intermediate are Hybrid/EGF-4 (28.9%),  $\beta$ -propeller/EGF-3 (15.9%),  $\beta$ -I/EGF-4 (11.5%), and  $\beta$ -propeller/Hybrid (8.8%). Three of these critical effective interactions involve EGF domains, and two involve the Hybrid and  $\beta$ -propeller domains, suggesting that the motions of these domains are rate limiting for integrin activation. Although flattening of the  $\beta$ -subunit knees is known to occur during integrin extension, the effective interactions between PSI/Calf-1 and between EGF-1/EGF-2 do not significantly contribute to the energy barrier for integrin activation (Figure 5e). The lower interaction surface of EGF-1/EGF-2 domains in the intermediate conformation with respect to the bent (Figure 3c) suggests that it is unlikely that the  $\beta$ -subunit knees play a major role in maintaining the bent structure. Previous studies of  $\alpha_{11b}\beta_3$  integrin and other isoforms have shown the importance of the  $\beta$ -propeller/Hybrid coupling in integrin activation (Gaillard et al., 2009; Puklin-Faucher et al., 2006; Su et al., 2022). Interestingly, in our study, the Hybrid and  $\beta$ -propeller domains were involved in the strongest pairwise interactions in both bent and intermediate hENMs (Figure 4c and Figure 4e); therefore, their average residue fluctuations were lower than those of the other domains (Figure 3a,b), suggesting that the Hybrid domain is a relatively rigid element (Shi et al., 2005).

It is worth noticing that the interdomain interactions that contribute most to the destabilization of the intermediate structure are not identical, although very similar, to those that contribute most to the energy barrier between bent and intermediate (Figure 5e,f). Although interaction energies between Hybrid/EGF-4,  $\beta$ -propeller/EGF-3, and  $\beta$ -I/EGF-4 are prominent in both decompositions,  $\beta$ -propeller/Hybrid does not contribute much to the intermediate energy destabilization (<0.1%), but it is a dominant contribution to the energy barrier between bent and intermediate states (Figure 5e,f). The difference in

the magnitude of interdomain effective interactions between bent and intermediate conformations implies that the interactions responsible for thermodynamic stabilization of the bent state are not necessarily involved in its kinetic stabilization and vice versa. Specifically, the contribution of  $\beta$ -propeller/Hybrid interaction is more critical before the intermediate is reached.

The values of energy extracted from equilibrium hENM harmonic interactions do not represent the exact energy barrier between conformations for two reasons. First, these values emerged in a process of weighted averaging of bent and intermediate structures (linear morphing, see Video S1). Based on this approach, all positions of the beads constituting the bent integrin model were moved toward the ones of the intermediate conformation along the shortest paths and using equal pace, therefore neglecting possible cooperative motions between domains that would allow to bypass the high-energy states and steric clashes. The energy magnitude is thus artificially inflated and semiquantitative. Despite this simplification of the transition pathway, this method still captures the relative contributions of all domain interactions to the conformational change. Second, hENMs are parametrized to match the near-equilibrium behavior from MD simulations and become less accurate away from the energy minimum. These two effects combine into the energy inflation along the morphing coordinate. However, we argue that at a semiquantitative level, the relative contributions of various domain-domain interactions are meaningful, as they emerge from the curvature of the energy in the earlier stages of transition and encode the displacements that are needed to transform one structure into the other.

Transitions between conformational states of large biological macromolecules are hard to capture by all-atom simulations. Approaches that prioritize computational efficiency over all-atom resolution, such as coarse-grained methods, can access longer time and length scales. However, previous CG models to study integrin activation either described the protein at a higher resolution (Bidone et al., 2019; Kalli et al., 2017; Tvaroška et al., 2023) or used a combination of manifold learning and deep generative modeling (Dasetty et al., 2023). Here, given the importance of domain motions in the allosteric regulation of proteins conformational transitions, we adopted a domain-resolution approach, where integrins are represented by only 14 beads with 12 corresponding to the extracellular domains. As all computational coarse-graining methods, our approach based on comparing the hENMs and linear morphing of two conformational states of a protein has its limitations. First, the hENM expression for the potential energy is tailored to represent the dynamics of a macromolecule in the vicinity of its stable conformation, and it does not accurately describe the energy of structures significantly distant from the stable conformation. Studies based on mixed elastic networks connected hENMs belonging to two conformational states of a protein to overcome this limitation (Zheng, 2008). However, although the mixed elastic network model smoothly interpolates the potential energy surface between the two minima, leading to a single expression describing protein in both stable states and in-between, the energy surface depends on additional parameters, such as mixing temperature and energy difference between minima of the two states (Zheng, 2008). Second, linear morphing itself is the simplest approach

to proposing a pathway for a conformational change (Weiss & Levitt, 2009). True reaction coordinates involve cooperation of a few independent degrees of freedom, drastically decreasing the transition energy, which is artificially inflated in our approach, and leading to complex motions. Nevertheless, our approach allowed us to single out what domain–domain interaction energies increase most quickly upon deformation and what energies destabilize the intermediate the most (Figure 5e,f), even if the precise energy values are merely semiquantitative. Therefore, the comparison of integrin hENMs allowed us to identify the effective interdomain interactions contributing to the kinetic and thermodynamic stability of integrin.

Although we limited our approach to all-atom and domain-resolution simulations, it is quite reasonable to expect that something in the middle, that is, coarse-graining with multiple grains per protein domain, would be an optimal approach for proteins of such complexity as integrin. In such a case, it is important to understand whether the grains themselves should be parameterized differently in various protein states, or whether they essentially retain their “identity” along the transitions. The intradomain analysis from this study shows that most domains fluctuate to a similar extent in bent and intermediate states (Figure 2a,b). However, there are notable counterexamples, including EGF-2, EGF-3, and EGF-4. Interestingly, domain sizes, as quantified by gyration radii (Figures S4 and S5), are conserved with respect to integrin extension. Considering the significance of the lower  $\beta$ -leg domains for integrin activation highlighted in this study, it will be interesting for future research to develop new coarse-grained models that incorporate the state-sensitivity of lower  $\beta$ -leg domains.

## 4 | MATERIALS AND METHODS

### 4.1 | All-atom MD simulations of membrane-embedded full-length $\alpha_{11b}\beta_3$ integrin

Residues that were missing in the cryo-EM reconstructions of bent and intermediate  $\alpha_{11b}\beta_3$  integrins (Xu et al., 2016) were first reconstructed. Positions of these residues were optimized using the Modeler (Fiser et al., 2000) loop refinement algorithm based on atomistic statistical potentials (see Supplementary information S1). Then, the completed full-length integrins were embedded within a lipid bilayer composed of DOPC + DOPS with a molar ratio of 3:1, using CHARMM-GUI membrane builder (Jo et al., 2009). Bent and intermediate  $\alpha_{11b}\beta_3$  integrins were oriented with the trans-membrane helix of the  $\alpha$  subunit perpendicular to the lipid bilayer, consistent with previous observations (Lau et al., 2008, 2009; Shattil et al., 2010). The membrane-embedded bent and intermediate integrins were then solvated using CHARMM-modified TIP3P water model (Huang et al., 2017; Jorgensen et al., 1983; Lee et al., 2016) and 150 mM NaCl, which served as counter ions to neutralize charges. Box dimensions were:  $\sim 15 \times 15 \times 24$  nm for the bent conformation, and  $\sim 12 \times 12 \times 26$  nm for the intermediate. In total, each system contained:  $\sim 523,000$  total atoms for the bent  $\alpha_{11b}\beta_3$  conformation,  $\sim 443,000$  atoms for the intermediate  $\alpha_{11b}\beta_3$  conformation.

Due to the large size of these systems, each conformation was subjected to a series of long equilibration stages before the final production run. The systems were energy minimized through steepest descent algorithm, followed by two consecutive equilibration simulations in the constant NVT ensemble (constant number of atoms,  $N$ ; volume,  $V$ ; and temperature,  $T$ ) and four consecutive equilibration simulations in the constant NPT ensemble (constant number of atoms,  $N$ ; pressure,  $P$ ; and temperature,  $T$ ), at 310 K. During the equilibration simulations, positional restraints were applied to both the protein and the lipid heavy atoms, and the dihedral angles. The first two equilibration simulations were run for 250 ps, with force constants between 956 and 95.6 kcal/(mol·nm<sup>2</sup>). The third equilibration simulation was also run for 250 ps, but with lower force constants, between 239 and 23.9 kcal/(mol·nm<sup>2</sup>). The last three equilibration simulations were run for 500 ps each, with decreasing backbone force constants from 1195 to 11.95 kcal/(mol·nm<sup>2</sup>), decreasing force constants from 47.8 to 0 kcal/(mol·nm<sup>2</sup>), for protein side chain atoms, lipid heavy atoms, and dihedral of lipid molecules. Production runs were then continued in the constant NPT ensemble at 310 K and 1 atm using the Nose-Hoover thermostat (Evans & Holian, 1985) and isotropic Parrinello-Rahman pressure coupling algorithm (Parrinello & Rahman, 1981). The length of covalent bonds involving hydrogen atoms was constrained using the Linear Constraint Solver (LINCS) algorithm (Hess et al., 1997), with integration time step of 2 fs. The Lennard-Jones interactions were cutoff at 1.2 nm with a switching function ranging from 1.0 to 1.2 nm, and the short-range electrostatic cutoff was set at 1.2 nm. The long-range electrostatic interactions were computed using the particle-mesh Ewald (PME) method with a 0.16 nm grid spacing (Darden et al., 1993). The highly scalable software GROMACS (version 2022.5, Abraham et al., 2015) and the force field CHARMM-36 m were adopted to run all equilibrium MD simulations until trajectories of 4.5  $\mu$ s were reached.

### 4.2 | All-atom MD simulations of the extracellular domains of $\alpha_{11b}\beta_3$ integrin

The 12 extracellular domains of integrin were extracted from bent  $\alpha_{11b}\beta_3$  and solvated using CHARMM-modified water model (Huang et al., 2017; Jorgensen et al., 1983; Lee et al., 2016) with 150 mM NaCl that were placed using the Monte Carlo method (Binder & Heermann, 2010a, 2010b) via CHARMM-GUI (Jo et al., 2008; Lee et al., 2016). The box sizes for each functional domain of  $\alpha_{11b}\beta_3$  integrin in solvent are provided in Table 1, and atom counts are provided in Table 2.

Each solvated domain was energy minimized using 5000 steps of steepest descent algorithm (Meza, 2010) and equilibrated for 125,000 steps, corresponding to 125 ps. Equilibration was performed in the constant NVT ensemble (constant number of atoms,  $N$ ; volume,  $V$ ; and temperature,  $T$ ), using positional restraints on the backbone and side chain atoms with force constants of 95.6 and 9.56 kcal/(mol·nm<sup>2</sup>), respectively. Production runs were then executed in the constant NPT ensemble (constant number of atoms,  $N$ ; pressure,  $P$ ; and temperature,  $T$ ), at 310 K and 1 atm using Parrinello-Rahman coupling (Parrinello & Rahman, 1981). The CHARMM-36 m force field was used for the

simulations. The PME (Darden et al., 1993) method was applied with a short-range cutoff of 1.2 nm to accommodate long-range electrostatic interactions. The LINCS (Hess et al., 1997) algorithm was used to restrict hydrogen bonds. The highly scalable software GROMACS (version 2022.5, Abraham et al., 2015) was adopted to run all equilibrium MD simulations until trajectories of 1  $\mu$ s were reached (500,000,000 steps).

VMD and PyMol were used for the visualization of the simulation trajectories (Delano, 2002; Humphrey et al., 1996). GROMACS native analysis tools, combined with our home-made scripts, were employed for the quantitative analysis of the trajectories.

### 4.3 | Statistical analysis of equilibrium MD simulations

To statistically compare time series of quantities from equilibrium MD simulations, such as RMSD, radius of gyration, and buried SASA, between isolated domains, domains embedded within bent integrin,

**TABLE 1** Box sizes for isolated extracellular domains of  $\alpha_{11b}\beta_3$  integrin.

Domain	X (nm)	Y (nm)	Z (nm)
$\beta$ -propeller	9.1	9.1	9.1
Thigh	8.1	8.1	8.1
Calf-1	7.3	7.3	7.3
Calf-2	9.3	9.3	9.3
PSI	5.3	5.3	5.3
Hybrid	7.2	7.2	7.2
$\beta$ -I	8.0	8.0	8.0
E1	5.9	5.9	5.9
E2	6.3	6.3	6.3
E3	5.0	5.0	5.0
E4	5.5	5.5	5.5
$\beta$ -TD	6.5	6.5	6.5

**TABLE 2** Atom counts for each isolated extracellular domain of  $\alpha_{11b}\beta_3$  integrin.

Domain	Protein (atom no.)	Na (atom no.)	Cl (atom no.)	H <sub>2</sub> O (atom no.)	Total atoms (no.)
$\beta$ -propeller	6774	75	60	63,219	70,128
Thigh	2380	45	44	47,070	49,539
Calf-1	2056	37	32	34,065	36,190
Calf-2	3437	76	68	71,907	75,488
PSI	828	15	12	12,987	13,842
Hybrid	2063	34	31	32,703	34,831
$\beta$ -I	3788	47	41	44,244	48,120
E1	572	20	17	18,489	19,098
E2	707	28	21	22,434	23,190
E3	488	12	10	10,980	11,490
E4	599	14	14	14,838	15,465
$\beta$ -TD	1339	28	22	24,114	25,503

and domains embedded within intermediate integrin, two-sample *t*-tests were performed. The *t*-tests were based on the null hypotheses that the time series of quantities have equal means, and the alternative hypotheses that they do not.

Time series we analyzed were substantially autocorrelated. To avoid artificially low standard errors due to autocorrelation, to obtain the standard errors, instead of dividing the pooled standard deviation of each quantity by the square root of the number of timeframes, we divided by the square root of *effective sample size* (Grossfield & Zuckerman, 2009; O'Shaughnessy & Cavanaugh, 2015). The *t*-value was computed as follows:

$$t = \frac{\langle X \rangle - \langle Y \rangle}{\sqrt{\frac{(n_X - 1)\sigma_X^2 + (n_Y - 1)\sigma_Y^2}{n_X + n_Y - 2}} \cdot \sqrt{\frac{1}{n_X} + \frac{1}{n_Y}}} \quad (2)$$

where  $\langle X/Y \rangle$  denote sample means over the time series,  $\sigma^2$  denote sample variances over the time series, and *n* stands for the effective sample sizes.

The *effective sample size* is an estimate of the number of statistically independent conformations throughout the trajectory and corresponds to the total number of timeframes divided by the average number of frames the autocorrelation substantially decreases. The autocorrelation was deemed gone when it decreased below  $1/e$  because, assuming exponential decay of autocorrelation, this value corresponds to the inverse of the coefficient multiplying time in the exponent. The effective sample sizes turned out to be orders of magnitude smaller than the number of simulation steps, which visibly increased the standard errors as compared with analysis of raw time series and disregarding the autocorrelation.

For the statistical analysis of RMSF, the trajectories were divided into 250 ns blocks, the RMSF was calculated for each block and the standard deviation was computed among the blocks. Dividing this value by the square root of 10 (number of blocks), a standard error was obtained. Standard errors and *p*-values from *t*-tests are reported in Figure 3.

#### 4.4 | Coarse-graining and heterogeneous elastic network modeling

The  $C_\alpha$  trajectories from all-atom MD simulations were mapped into coarse-grained trajectories with 12 beads representing the extracellular domains and 2 beads representing the transmembrane helices. The beads were positioned in the geometric centers of the corresponding groups of  $C_\alpha$ , as reported in Table 3. Mapping was performed using OpenMSCG cgmmap tool (Peng et al., 2023). hENMs were parameterized (Lyman et al., 2008) using a potential energy  $V$  expressed by a diagonal quadratic form of interdomain distances  $r_{ij}$ :

$$V(\{r_{ij}\}; \{k_{ij}\}, \{r_{0,ij}\}) = \sum_{i < j} k_{ij} (r_{ij} - r_{0,ij})^2 \quad (3)$$

The OpenMSCG cghenm tool (Peng et al., 2023) was used to determine force constants  $k_{ij}$  and equilibrium distances  $r_{0,ij}$  for all domain pairs. We did not use any spatial cutoff while parameterizing hENMs, and set the temperature to 310 K. All parameters for cghenm are listed in Table 4.

This approach is based on structural dynamic correlations between beads and ensures that the domain fluctuations observed in coarse-grained MD trajectories were reproduced by coarse-grained model. Starting from the all-atom trajectories of the beads between 2 and 4.5  $\mu$ s of equilibrium MD simulation, the hENM approach iteratively performs four steps. The first step is to assign to all pairs of beads a uniform spring constant. The second step is to relax the positions of the beads using a steepest-descent search, then compute the normal modes and scale their amplitudes according to equipartition of energy. The third step is to project the fluctuations computed from the normal-mode analysis onto the distance vectors of all pairs of beads. The fourth step is to update all spring constants simultaneously

**TABLE 3** List of the extracellular domains of integrin with their respective residue numbers.

Domain	Residue start	Residue end
$\beta$ -propeller	1	452
Thigh	453	608
Calf-1	609	743
Calf-2	744	964
PSI	1009	1065
Hybrid	1066	1117
	1361	1440
$\beta$ -I	1118	1360
E1	1441	1483
E2	1484	1533
E3	1534	1568
E4	1569	1612
$\beta$ -TD	1613	1698

based on minimizing the difference between normal mode and MD fluctuations. The algorithm repeats steps 2–4 until the difference between the normal-mode fluctuations and target MD fluctuations is below a predefined threshold.

#### 4.5 | Brownian dynamics simulations

The hENM potential energy functions were used to model the interdomain interactions of bent and intermediate hENM models. The CG models were propagated using BD (Ermak & McCammon, 1978; Huber & McCammon, 2019) in LAMMPS (Thompson et al., 2022), with the forward Euler propagation scheme:

$$x(t + \Delta t) = x(t) + \gamma^{-1} F \Delta t + \sqrt{2k_B T \Delta t / \gamma} X \quad (4)$$

where  $x$  is the particle's position,  $\gamma$  is its friction coefficient,  $t$  is time,  $\Delta t$  is simulation timestep,  $F$  is force (negative gradient of the potential energy given by equation 3),  $k_B$  is Boltzmann constant,  $T$  is temperature and  $X$  is a standard normal random variable.

The temperature was set to 310 K, timestep to 0.1 ps, total simulation time to 100  $\mu$ s, and each bead was assigned a friction coefficient of 20 g/mol/fs, which assuming viscosity of  $\sim 1$  cP (viscosity of water) corresponds to hydrodynamic radius of 1.75 nm. This value is comparable to the gyration radii of domains reported in Figures S4 and S5. It is worth noting that friction coefficient  $\gamma$  steers the magnitude of random and damping forces, but does not affect the equilibrium distributions, because in the propagation scheme it is multiplied by the timestep  $\Delta t$  (Ermak & McCammon, 1978). Thus, changing friction is equivalent to merely rescaling a time unit. Trajectory analysis was performed using the MDAnalysis python library (Gowers et al., 2016; Michaud-Agrawal et al., 2011). In the BD simulations, we do not explicitly restrict the mobility of the beads representing membrane-spanning helices. However, their motion implicitly considers the presence of the plasma membrane, as their interaction potentials with other beads match fluctuations with membrane-embedded all-atom equilibrium conformations.

**TABLE 4** Parameters used in heterogeneous elastic network modeling.

Parameter	Value
Temperature (K)	310
Cutoff of bonds ( $\text{\AA}$ )	300
Convergence factor (mol/kcal)	0.1
Max number of iterations	100,000
Tolerance of $k$ -constants (kcal/mol/ $\text{\AA}^2$ )	0.0001
Step size for steepest descent minimization	1.0
Max number of steps in steepest descent minimization	10,000
Tolerance of forces in steepest descent minimization	0.00001



## 4.6 | Variations of the hENM potential energy expression

To assess the role of the interdomain interactions on the transition from bent to intermediate integrin, the pairwise potentials of bent hENM were varied as follows: first, the potential energy expression of the intermediate hENM was applied to the bent conformation (*swapped hENM*); second, selected “stabilizing” interactions of bent hENM were turned off (*reduced hENM*); and last, the potential energy expression for the intermediate hENM was applied to the bent conformation with interactions stabilizing bent hENM turned off (*both*).

To identify “stabilizing” interactions, a dimensionless displacement  $\Delta\tilde{r}$  was used by analogy with natural oscillator units expressing displacements between quantum harmonic oscillator minima relevant for UV-Vis spectroscopy (Atkins & Friedman, 2005).  $\Delta\tilde{r}$  was defined as:

$$\Delta\tilde{r} = \sqrt{\frac{k}{k_B T}} \Delta r, \quad (5)$$

where  $k$  denotes force constant,  $k_B$  is Boltzmann constant,  $T$  is temperature, and  $\Delta r = r_{0,\text{int}} - r_{0,\text{bent}}$  is the difference between equilibrium distances in intermediate and bent conformations. Following that definition,  $\Delta\tilde{r}^2$  expresses the energy in  $k_B T$  units needed to stretch a given harmonic bond from its equilibrium length in bent state up to its equilibrium length in the intermediate state, which is high if either force constant or difference in equilibrium distances is high. When  $\Delta\tilde{r} < 1$ , the energetic cost for this change is  $\sim k_B T$  or less; when  $\Delta\tilde{r} \gg 1$ , the energetic cost is  $\gg k_B T$ . The reduced hENM was defined as a bent hENM where the interactions presenting  $\Delta\tilde{r} > 3$  were turned off.

## 4.7 | Linear morphing of integrin conformation and assessment of total energy

To gain insights into the energy barriers underlying integrin extension, a sequence of conformations was generated starting from the positions of domains in bent and intermediate conformations and using linear morphing. The morphing sequence was generated using:

$$x_\lambda = (1 - \lambda)x_{\text{bent}} + \lambda x_{\text{int}}, \quad (6)$$

where  $\lambda \in [0, 1]$  is the morphing degree and  $x$  represents the positions of domains in the respective structures.

To avoid dependence on a transient configuration of domains, instead of picking a single bent-intermediate structure pair for linear morphing, multiple pairs were extracted from MD simulations at times 2.5–3.5  $\mu\text{s}$  every 0.2  $\mu\text{s}$  and then morphed, that is, linearly interpolated with  $\lambda$  incremented by 0.05. The potential energy as a function of  $\lambda$  was calculated using different potential energy expressions, namely: hENM for bent integrin, hENM for intermediate, reduced hENM for the bent conformation and reduced hENM for the intermediate conformation and averaged over multiple morphing pairs.

To select interactions that contribute: (i) to the energy barrier upon morphing the bent conformation into intermediate ( $\lambda = 0.5$ ),

and (ii) to the stabilization of the intermediate conformation ( $\lambda = 1$ ), each quadratic term of Equation (3) was separately evaluated using bent hENM parametrization, and then divided by their sum.

## AUTHOR CONTRIBUTIONS

*Study conception and design:* T.C.B and R.D.R. *MD simulations and analysis:* O.J. and A.Y. *Coarse-graining, BD, and comparative analysis between CG systems:* T.S. *Data collection:* O.J, A.Y., and T.S. *Analysis and interpretation of the results:* T.S., R.D.R, and T.C.B. *Draft article preparation:* O.J., A.Y., and T.S. All authors reviewed the results and approved the final version of the article.

## ACKNOWLEDGMENTS

This work was supported by the National Institute of Health, grant number: 1R35GM147491-01. Computer time was provided by the Scientific Computing and Imaging Institute and the Center for High Performance Computing at the University of Utah. We acknowledge Dr. Robert Coffman and Reza Kolasangiani for assistance with MD simulations.

## CONFLICT OF INTEREST STATEMENT

The authors declare no conflicts of interest.

## DATA AVAILABILITY STATEMENT

The data that support the findings of this study are openly available in `alphalBbeta3_bent_int_transition` at <https://github.com/tamarabidone/>.

## ORCID

Tamara C. Bidone  <https://orcid.org/0000-0002-7096-4839>

## REFERENCES

- Abraham, M. J., Murtola, T., Schulz, R., Páll, S., Smith, J. C., Hess, B., & Lindahl, E. (2015). GROMACS: High performance molecular simulations through multi-level parallelism from laptops to supercomputers. *SoftwareX*, 1–2, 19–25. <https://doi.org/10.1016/j.softx.2015.06.001>
- Adair, B. D., & Yeager, M. (2002). Three-dimensional model of the human platelet integrin  $\alpha\text{IIb}\beta\text{3}$  based on electron cryomicroscopy and x-ray crystallography. *Proceedings of the National Academy of Sciences of the United States of America*, 99(22), 14059–14064. <https://doi.org/10.1073/pnas.212498199>
- Atkins, P. W., & Friedman, R. S. (2005). *Linear motion and the harmonic oscillator*. In *Molecular Quantum Mechanics*, Fourth Edition (pp. 60–65). Oxford University Press.
- Barton, S. J., Travis, M. A., Askari, J. A., Buckley, P. A., Craig, S. E., Humphries, M. J., & Mould, A. P. (2004). Novel activating and inactivating mutations in the integrin beta1 subunit a domain. *Biochemical Journal*, 380(Pt 2), 401–407. <https://doi.org/10.1042/BJ20031973>
- Bennett, J. S. (2005). Structure and function of the platelet integrin  $\alpha\text{IIb}\beta\text{3}$ . *Journal of Clinical Investigation*, 115(12), 3363–3369. <https://doi.org/10.1172/JCI26989>
- Bennett, J. S., Berger, B. W., & Billings, P. C. (2009). The structure and function of platelet integrins. *Journal of Thrombosis and Haemostasis: JTH*, 7(Suppl 1), 200–205. <https://doi.org/10.1111/j.1538-7836.2009.03378.x>
- Bhatt, D. L., & Topol, E. J. (2003). Scientific and therapeutic advances in antiplatelet therapy. *Nature Reviews Drugs Discovery*, 2, 15–28.
- Bidone, T. C., Polley, A., Jin, J., Driscoll, T., Iwamoto, D. V., Calderwood, D. A., Schwartz, M. A., & Voth, G. A. (2019). Coarse-grained simulation of full-length integrin activation. *Biophysical Journal*, 116(6), 1000–1010. <https://doi.org/10.1016/j.bpj.2019.02.011>

- Binder, K., & Heermann, D. W. (2010a). *Monte Carlo simulation in statistical physics* (4th ed.). Springer-Verlag. <https://doi.org/10.1007/978-3-662-04685-2>
- Binder, K., & Heermann, D. W. (2010b). *Monte Carlo simulation in statistical physics: An introduction*. Springer. <https://doi.org/10.1007/978-3-642-03163-2>
- Botero, J. P., Lee, K., Branchford, B. R., Bray, P. F., Freson, K., Lambert, M. P., Luo, M., Mohan, S., Ross, J. E., Bergmeier, W., Di Paola, J., & ClinGen Platelet Disorder Variant Curation Expert Panel. (2020). Glanzmann thrombasthenia: Genetic basis and clinical correlates. *Haematologica*, 105(4), 888–894. <https://doi.org/10.3324/haematol.2018.214239>
- Bouvard, D., Pouwels, J., De Franceschi, N., & Ivaska, J. (2013). Integrin inactivators: Balancing cellular functions in vitro and in vivo. *Nature Reviews. Molecular Cell Biology*, 14(7), 430–442. <https://doi.org/10.1038/nrm3599>
- Campbell, I. D., & Humphries, M. J. (2011). Integrin structure, activation, and interactions. *Cold Spring Harbor Perspectives in Biology*, 3(3), a004994. <https://doi.org/10.1101/cshperspect.a004994>
- Chen, C. S. (2008). Mechanotransduction—A field pulling together? *Journal of Cell Science*, 121(Pt 20), 3285–3292. <https://doi.org/10.1242/jcs.023507>
- Chen, Y., Ju, L. A., Zhou, F., Liao, J., Xue, L., Su, Q. P., Jin, D., Yuan, Y., Lu, H., Jackson, S. P., & Zhu, C. (2019). An integrin  $\alpha$ IIb $\beta$ 3 intermediate affinity state mediates biomechanical platelet aggregation. *Nature Materials*, 18(7), 760–769. <https://doi.org/10.1038/s41563-019-0323-6>
- Chen, Y., Li, Z., Kong, F., Ju, L. A., & Zhu, C. (2023). Force-regulated spontaneous conformational changes of integrins  $\alpha$ 5 $\beta$ 1 and  $\alpha$ V $\beta$ 3. *ACS Nano*, 18(1), 299–313. <https://doi.org/10.1021/acsnano.3c06253>
- Darden, T., York, D., & Pedersen, L. (1993). Particle mesh Ewald: An N-log(N) method for Ewald sums in large systems. *The Journal of Chemical Physics*, 98(12), 10089–10092. <https://doi.org/10.1063/1.464397>
- Dasety, S., Bidone, T. C., & Ferguson, A. L. (2023). Data-driven prediction of  $\alpha$ IIb $\beta$ 3 integrin activation paths using manifold learning and deep generative modeling. *Biophysical Journal*. <https://doi.org/10.1016/j.bpj.2023.12.009>
- Delano, W. L. (2002). The PyMOL molecular graphics system.
- Ermak, D. L., & McCammon, J. A. (1978). Brownian dynamics with hydrodynamic interactions. *The Journal of Chemical Physics*, 69(4), 1352–1360. <https://doi.org/10.1063/1.436761>
- Evans, D. J., & Holian, B. L. (1985). The Nose–Hoover thermostat. *The Journal of Chemical Physics*, 83(8), 4069–4074. <https://doi.org/10.1063/1.449071>
- Fiser, A., Do, R. K., & Sali, A. (2000). Modeling of loops in protein structures. *Protein Science: A Publication of the Protein Society*, 9(9), 1753–1773. <https://doi.org/10.1110/ps.9.9.1753>
- Friedland, J. C., Lee, M. H., & Boettiger, D. (2009). Mechanically activated integrin switch controls  $\alpha$ 5 $\beta$ 1 function. *Science, New York, N.Y.*, 323(5914), 642–644. <https://doi.org/10.1126/science.1168441>
- Gaillard, T., Dejaegere, A., & Stote, R. H. (2009). Dynamics of  $\beta$ 3 integrin I-like and hybrid domains: Insight from simulations on the mechanism of transition between open and closed forms. *Proteins: Structure, Function, and Bioinformatics*, 76(4), 977–994. <https://doi.org/10.1002/prot.22404>
- Gowers, R., Linke, M., Barnoud, J., Reddy, T., Melo, M., Seyler, S. L., Domański, J., Dotson, D. L., Buchoux, S., Kenney, I. M., & Beckstein, O. (2016, January 1). MDAnalysis: A Python package for the rapid analysis of molecular dynamics simulations, 98–105 <https://doi.org/10.25080/Majora-629e541a-00e>
- Grossfield, A., & Zuckerman, D. M. (2009). Quantifying uncertainty and sampling quality in biomolecular simulations. *Annual Reports in Computational Chemistry*, 5, 23–48. [https://doi.org/10.1016/S1574-1400\(09\)00502-7](https://doi.org/10.1016/S1574-1400(09)00502-7)
- Hanein, D., & Volkman, N. (2018). Conformational equilibrium of human platelet integrin investigated by three-dimensional electron Cryo-microscopy. *Sub-Cellular Biochemistry*, 87, 353–363. [https://doi.org/10.1007/978-981-10-7757-9\\_12](https://doi.org/10.1007/978-981-10-7757-9_12)
- Hess, B., Bekker, H., Berendsen, H. J. C., & Fraaije, J. G. E. M. (1997). LINC: A linear constraint solver for molecular simulations. *Journal of Computational Chemistry*, 18(12), 1463–1472. [https://doi.org/10.1002/\(sici\)1096-987x\(199709\)18:12<1463::aid-jcc4>3.0.co;2-h](https://doi.org/10.1002/(sici)1096-987x(199709)18:12<1463::aid-jcc4>3.0.co;2-h)
- Hilser, V. J., & Thompson, E. B. (2007). Intrinsic disorder as a mechanism to optimize allosteric coupling in proteins. *Proceedings of the National Academy of Sciences of the United States of America*, 104(20), 8311–8315. <https://doi.org/10.1073/pnas.0700329104>
- Huang, J., Rauscher, S., Nawrocki, G., Ran, T., Feig, M., de Groot, B. L., Grubmüller, H., & MacKerell, A. D., Jr. (2017). CHARMM36m: An improved force field for folded and intrinsically disordered proteins. *Nature Methods*, 14(1), 71–73. <https://doi.org/10.1038/nmeth.4067>
- Huber, G. A., & McCammon, J. A. (2019). Brownian dynamics simulations of biological molecules. *Trends in Chemistry*, 1(8), 727–738. <https://doi.org/10.1016/j.trechm.2019.07.008>
- Humphrey, W., Dalke, A., & Schulten, K. (1996). VMD: Visual molecular dynamics. *Journal of Molecular Graphics*, 14(1), 33–38. [https://doi.org/10.1016/0263-7855\(96\)00018-5](https://doi.org/10.1016/0263-7855(96)00018-5)
- Huo, T., Hongjiang, W., Moussa, Z., Sen, M., Dalton, V., & Wang, Z. (2024). Full-length  $\alpha$ IIb $\beta$ 3 cryo-EM structure reveals intact integrin initiate-activation intrinsic architecture. *Structure*, 32, 1–8. <https://doi.org/10.1016/j.str.2024.03.006>
- Hynes, R. O. (2002). Integrins: Bidirectional, allosteric signaling machines. *Cell*, 110(6), 673–687. [https://doi.org/10.1016/S0092-8674\(02\)00971-6](https://doi.org/10.1016/S0092-8674(02)00971-6)
- Jackson, S. P. (2011). Arterial thrombosis—Insidious, unpredictable and deadly. *Nature Medicine*, 17(11), 1423–1436. <https://doi.org/10.1038/nm.2515>
- Jallu, V., Poulain, P., Fuchs, P. F. J., Kaplan, C., & de Brevern, A. G. (2012). Modeling and Molecular Dynamics of HPA-1a and -1b Polymorphisms: Effects on the Structure of the  $\beta$ 3 Subunit of the  $\alpha$ IIb $\beta$ 3 Integrin. *PLoS ONE*, 7(11), e47304. <https://doi.org/10.1371/journal.pone.0047304>
- Jo, S., Kim, T., Iyer, V. G., & Im, W. (2008). CHARMM-GUI: A web-based graphical user interface for CHARMM. *Journal of Computational Chemistry*, 29(11), 1859–1865. <https://doi.org/10.1002/jcc.20945>
- Jo, S., Lim, J. B., Klauda, J. B., & Im, W. (2009). CHARMM-GUI membrane builder for mixed bilayers and its application to yeast membranes. *Biophysical Journal*, 97(1), 50–58. <https://doi.org/10.1016/j.bpj.2009.04.013>
- Jorgensen, W. L., Chandrasekhar, J., Madura, J. D., Impey, R. W., & Klein, M. L. (1983). Comparison of simple potential functions for simulating liquid water. *The Journal of Chemical Physics*, 79(2), 926–935. <https://doi.org/10.1063/1.445869>
- Kabsch, W. (1978). A discussion of the solution for the best rotation to relate two sets of vectors. *Acta Crystallographica Section A: Crystal Physics, Diffraction, Theoretical and General Crystallography*, 34(5), 827–828. <https://doi.org/10.1107/S0567739478001680>
- Kalli, A. C., Rog, T., Vattulainen, I., Campbell, I. D., & Sansom, M. S. P. (2017). The integrin receptor in biologically relevant bilayers: Insights from molecular dynamics simulations. *The Journal of Membrane Biology*, 250(4), 337–351. <https://doi.org/10.1007/s00232-016-9908-z>
- Kamata, T., Handa, M., Ito, S., Sato, Y., Ohtani, T., Kawai, Y., Ikeda, Y., & Aiso, S. (2010). Structural requirements for activation in  $\alpha$ IIb $\beta$ 3 integrin. *The Journal of Biological Chemistry*, 285(49), 38428–38437. <https://doi.org/10.1074/jbc.M110.139667>
- Kolasangani, R., Bidone, T. C., & Schwartz, M. A. (2022). Integrin conformational dynamics and mechanotransduction. *Cells*, 11(22), 3584. <https://doi.org/10.3390/cells11223584>
- Kong, F., García, A. J., Mould, A. P., Humphries, M. J., & Zhu, C. (2009). Demonstration of catch bonds between an integrin and its ligand. *The Journal of Cell Biology*, 185(7), 1275–1284. <https://doi.org/10.1083/jcb.200810002>
- Kroll, M. H., Hellums, J. D., McIntire, L. V., Schafer, A. I., & Moake, J. L. (1996). Platelets and shear stress. *Blood*, 88(5), 1525–1541.

- Lau, T.-L., Dua, V., & Ulmer, T. S. (2008). Structure of the integrin  $\alpha$ IIb transmembrane segment. *The Journal of Biological Chemistry*, 283(23), 16162–16168. <https://doi.org/10.1074/jbc.M801748200>
- Lau, T.-L., Kim, C., Ginsberg, M. H., & Ulmer, T. S. (2009). The structure of the integrin  $\alpha$ IIb $\beta$ 3 transmembrane complex explains integrin transmembrane signalling. *The EMBO Journal*, 28(9), 1351–1361. <https://doi.org/10.1038/emboj.2009.63>
- Lee, J., Cheng, X., Swails, J. M., Yeom, M. S., Eastman, P. K., Lemkul, J. A., Wei, S., Buckner, J., Jeong, J. C., Qi, Y., Jo, S., Pande, V. S., Case, D. A., Brooks, C. L., 3rd, MacKerell, A. D., Jr., Klauda, J. B., & Im, W. (2016). CHARMM-GUI input generator for NAMD, GROMACS, AMBER, OpenMM, and CHARMM/OpenMM simulations using the CHARMM36 additive force field. *Journal of Chemical Theory and Computation*, 12(1), 405–413. <https://doi.org/10.1021/acs.jctc.5b00935>
- Li, Z., Delaney, M. K., O'Brien, K. A., & Du, X. (2010). Signaling during platelet adhesion and activation. *Arteriosclerosis, Thrombosis, and Vascular Biology*, 30(12), 2341–2349. <https://doi.org/10.1161/ATVBAHA.110.207522>
- Luo, B.-H., Springer, T. A., & Takagi, J. (2003). Stabilizing the open conformation of the integrin headpiece with a glycan wedge increases affinity for ligand. *Proceedings of the National Academy of Sciences of the United States of America*, 100(5), 2403–2408. <https://doi.org/10.1073/pnas.0438060100>
- Lyman, E., Pfaendtner, J., & Voth, G. A. (2008). Systematic multiscale parameterization of heterogeneous elastic network models of proteins. *Biophysical Journal*, 95(9), 4183–4192. <https://doi.org/10.1529/biophysj.108.139733>
- Ma, Y.-Q., Qin, J., & Plow, E. F. (2007). Platelet integrin  $\alpha$ IIb $\beta$ 3: Activation mechanisms. *Journal of Thrombosis and Haemostasis*, 5(7), 1345–1352. <https://doi.org/10.1111/j.1538-7836.2007.02537.x>
- Meza, J. C. (2010). Steepest descent. *Wiley Interdisciplinary Reviews: Computational Statistics*, 2(6), 719–722. doi:10.1002/wics.117
- Michaud-Agrawal, N., Denning, E. J., Woolf, T. B., & Beckstein, O. (2011). MDAAnalysis: A toolkit for the analysis of molecular dynamics simulations. *Journal of Computational Chemistry*, 32(10), 2319–2327. <https://doi.org/10.1002/jcc.21787>
- Motlagh, H. N., Wrabl, J. O., Li, J., & Hilser, V. J. (2014). The ensemble nature of allostery. *Nature*, 508(7496), 331–339. <https://doi.org/10.1038/nature13001>
- Moore, T. I., Aaron, J., Chew, T.-L., & Springer, T. A. (2018). Measuring integrin conformational change on the cell surface with super-resolution microscopy. *Cell Reports*, 22(7), 1903–1912. <https://doi.org/10.1016/j.celrep.2018.01.062>
- Mould, A. P., Akiyama, S. K., & Humphries, M. J. (1995). Regulation of integrin  $\alpha$ 5  $\beta$ 1-fibronectin interactions by divalent cations. Evidence for distinct classes of binding sites for Mn<sup>2+</sup>, Mg<sup>2+</sup>, and Ca<sup>2+</sup>. *The Journal of Biological Chemistry*, 270(44), 26270–26277. <https://doi.org/10.1074/jbc.270.44.26270>
- Mould, A. P., Barton, S. J., Askari, J. A., McEwan, P. A., Buckley, P. A., Craig, S. E., & Humphries, M. J. (2003). Conformational changes in the integrin beta domain provide a mechanism for signal transduction via hybrid domain movement. *The Journal of Biological Chemistry*, 278(19), 17028–17035. <https://doi.org/10.1074/jbc.M213139200>
- Nesbitt, W. S., Kulkarni, S., Giuliano, S., Goncalves, I., Dopheide, S. M., Yap, C. L., Harper, I. S., Salem, H. H., & Jackson, S. P. (2002). Distinct glycoprotein Ib/V/IX and integrin  $\alpha$ IIb $\beta$ 3-dependent calcium signals cooperatively regulate platelet adhesion under flow. *The Journal of Biological Chemistry*, 277(4), 2965–2972. <https://doi.org/10.1074/jbc.M110070200>
- Nesbitt, W. S., Westein, E., Tovar-Lopez, F. J., Tolouei, E., Mitchell, A., Fu, J., Carberry, J., Fouras, A., & Jackson, S. P. (2009). A shear gradient-dependent platelet aggregation mechanism drives thrombus formation. *Nature Medicine*, 15(6), 665–673. <https://doi.org/10.1038/nm.1955>
- Nishida, N., Xie, C., Shimaoka, M., Cheng, Y., Walz, T., & Springer, T. A. (2006). Activation of leukocyte  $\beta$ 2 integrins by conversion from bent to extended conformations. *Immunity*, 25(4), 583–594. <https://doi.org/10.1016/j.immuni.2006.07.016>
- O'Shaughnessy, P., & Cavanaugh, J. E. (2015). Performing T-tests to compare autocorrelated time series data collected from direct-reading instruments. *Journal of Occupational and Environmental Hygiene*, 12(11), 743–752. <https://doi.org/10.1080/15459624.2015.1044603>
- Parise, L. V. (1999). Integrin  $\alpha$ IIb $\beta$ 3 signaling in platelet adhesion and aggregation. *Current Opinion in Cell Biology*, 11(5), 597–601. [https://doi.org/10.1016/s0955-0674\(99\)00018-6](https://doi.org/10.1016/s0955-0674(99)00018-6)
- Parrinello, M., & Rahman, A. (1981). Polymorphic transitions in single crystals: A new molecular dynamics method. *Journal of Applied Physics*, 52(12), 7182–7190. <https://doi.org/10.1063/1.3288693>
- Paszek, M. J., & Weaver, V. M. (2004). The tension mounts: Mechanics meets morphogenesis and malignancy. *Journal of Mammary Gland Biology and Neoplasia*, 9(4), 325–342. <https://doi.org/10.1007/s10911-004-1404-x>
- Payraastre, B., Missy, K., Trumel, C., Bodin, S., Plantavid, M., & Chap, H. (2000). The integrin  $\alpha$ IIb $\beta$ 3 in human platelet signal transduction. *Biochemical Pharmacology*, 60(8), 1069–1074. [https://doi.org/10.1016/S0006-2952\(00\)00417-2](https://doi.org/10.1016/S0006-2952(00)00417-2)
- Peng, Y., Pak, A. J., Durumeric, A. E. P., Sahrman, P. G., Mani, S., Jin, J., Loose, T. D., Beiter, J., & Voth, G. A. (2023). OpenMSCG: A software tool for bottom-up coarse-graining. *The Journal of Physical Chemistry B*, 127(40), 8537–8550. <https://doi.org/10.1021/acs.jpcc.3c04473>
- Puklin-Faucher, E., Gao, M., Schulten, K., & Vogel, V. (2006). How the headpiece hinge angle is opened: New insights into the dynamics of integrin activation. *The Journal of Cell Biology*, 175(2), 349–360. <https://doi.org/10.1083/jcb.200602071>
- Puklin-Faucher, E., & Sheetz, M. P. (2009). The mechanical integrin cycle. *Journal of Cell Science*, 122(Pt 2), 179–186. <https://doi.org/10.1242/jcs.042127>
- Puklin-Faucher, E., & Vogel, V. (2009). Integrin activation dynamics between the RGD-binding site and the headpiece hinge. *The Journal of Biological Chemistry*, 284(52), 36557–36568. <https://doi.org/10.1074/jbc.M109.041194>
- Schumacher, S., Dedden, D., Nunez, R. V., Matoba, K., Takagi, J., Biertümpfel, C., & Mizuno, N. (2021). Structural insights into integrin  $\alpha$ 5 $\beta$ 1 opening by fibronectin ligand. *Science Advances*, 7(19), 9716. <https://doi.org/10.1126/sciadv.abe9716>
- Shattil, S. J., Hoxie, J. A., Cunningham, M., & Brass, L. F. (1985). Changes in the platelet membrane glycoprotein IIb/IIIa complex during platelet activation. *The Journal of Biological Chemistry*, 260(20), 11107–11114.
- Shattil, S. J., Kashiwagi, H., & Pampori, N. (1998). Integrin signaling: The platelet paradigm. *Blood*, 91(8), 2645–2657. [https://doi.org/10.1182/blood.V91.8.2645.2645\\_2645\\_2657](https://doi.org/10.1182/blood.V91.8.2645.2645_2645_2657)
- Shattil, S. J., Kim, C., & Ginsberg, M. H. (2010). The final steps of integrin activation: The end game. *Nature Reviews. Molecular Cell Biology*, 11(4), 288–300. <https://doi.org/10.1038/nrm2871>
- Shen, B., Zhao, X., O'Brien, K. A., Stojanovic-Terpo, A., Delaney, M. K., Kim, K., Cho, J., Lam, S. C., & Du, X. (2013). A directional switch of integrin signalling and a new anti-thrombotic strategy. *Nature*, 503(7474), 131–135. <https://doi.org/10.1038/nature12613>
- Shi, M., Sundramurthy, K., Liu, B., Tan, S.-M., Law, S. K. A., & Lescar, J. (2005). The crystal structure of the plexin-Semaphorin-integrin domain/hybrid domain/I-EGF1 segment from the human integrin  $\beta$ 2 subunit at 1.8-Å resolution. *Journal of Biological Chemistry*, 280(34), 30586–30593. <https://doi.org/10.1074/jbc.M502525200>
- Smaghe, B. J., Huang, P.-S., Ban, Y.-E. A., Baker, D., & Springer, T. A. (2010). Modulation of integrin activation by an entropic spring in the  $\beta$ -knee. *The Journal of Biological Chemistry*, 285(43), 32954–32966. <https://doi.org/10.1074/jbc.M110.145177>
- Springer, T. A., Zhu, J., & Xiao, T. (2008). Structural basis for distinctive recognition of fibrinogen  $\gamma$ C peptide by the platelet integrin  $\alpha$ IIb $\beta$ 3. *The Journal of Cell Biology*, 182(4), 791–800. <https://doi.org/10.1083/jcb.200801146>

- Stalker, T. J., Traxler, E. A., Wu, J., Wannemacher, K. M., Cermignano, S. L., Voronov, R., Diamond, S. L., & Brass, L. F. (2013). Hierarchical organization in the hemostatic response and its relationship to the platelet-signaling network. *Blood*, 121(10), 1875–1885. <https://doi.org/10.1182/blood-2012-09-457739>
- Su, Y., Iacob, R. E., Li, J., Engen, J. R., & Springer, T. A. (2022). Dynamics of integrin  $\alpha 5\beta 1$ , fibronectin, and their complex reveal sites of interaction and conformational change. *The Journal of Biological Chemistry*, 298(9), 102323. <https://doi.org/10.1016/j.jbc.2022.102323>
- Takagi, J., Petre, B. M., Walz, T., & Springer, T. A. (2002). Global conformational rearrangements in integrin extracellular domains in outside-in and inside-out signaling. *Cell*, 110(5), 599–611. [https://doi.org/10.1016/S0092-8674\(02\)00935-2](https://doi.org/10.1016/S0092-8674(02)00935-2)
- Takagi, J., Strokovich, K., Springer, T. A., & Walz, T. (2003). Structure of integrin  $\alpha 5\beta 1$  in complex with fibronectin. *The EMBO Journal*, 22(18), 4607–4615. <https://doi.org/10.1093/emboj/cdg445>
- Tello-Montoliu, A., Jover, E., Rivera, J., Valdés, M., Angiolillo, D. J., & Marín, F. (2012). New perspectives in antiplatelet therapy. *Current Medicinal Chemistry*, 19(3), 406–427. <https://doi.org/10.2174/092986712803414240>
- Thompson, A. P., Aktulga, H. M., Berger, R., Bolintineanu, D. S., Brown, W. M., Crozier, P. S., in 't Veld, P. J., Kohlmeyer, A., Moore, S. G., Nguyen, T. D., Shan, R., Stevens, M. J., Tranchida, J., Trott, C., & Plimpton, S. J. (2022). LAMMPS—flexible simulation tool for particle-based materials modeling at the atomic, meso, and continuum scales. *Computer Physics Communications*, 271, 108171. <https://doi.org/10.1016/j.cpc.2021.108171>
- Tong, D., Soley, N., Kolasangiani, R., Schwartz, M. A., & Bidone, T. C. (2023). Integrin  $\alpha 11\beta 3$  intermediates: From molecular dynamics to adhesion assembly. *Biophysical Journal*, 122(3), 533–543. <https://doi.org/10.1016/j.bpj.2022.12.032>
- Tvaroška, I., Kozmon, S., & Kóňa, J. (2023). Molecular modeling insights into the structure and behavior of integrins: A review. *Cells*, 12(2), 324. <https://doi.org/10.3390/cells12020324>
- Weiss, D. R., & Levitt, M. (2009). Can morphing methods predict intermediate structures? *Journal of Molecular Biology*, 385(2), 665–674. <https://doi.org/10.1016/j.jmb.2008.10.064>
- Xiao, T., Takagi, J., Collier, B. S., Wang, J.-H., & Springer, T. A. (2004). Structural basis for allostery in integrins and binding to fibrinogen-mimetic therapeutics. *Nature*, 432(7013), 59–67. <https://doi.org/10.1038/nature02976>
- Xin, H., Huang, J., Song, Z., Mao, J., Xi, X., & Shi, X. (2023). Structure, signal transduction, activation, and inhibition of integrin  $\alpha 11\beta 3$ . *Thrombosis Journal*, 21(1). <https://doi.org/10.1186/s12959-023-00463-w>
- Xiong, J.-P., Stehle, T., Diefenbach, B., Zhang, R., Dunker, R., Scott, D. L., Joachimiak, A., Goodman, S. L., & Arnaout, M. A. (2001). Crystal structure of the extracellular segment of integrin  $\alpha V\beta 3$ . *Science*, 294(5541), 339–345. <https://doi.org/10.1126/science.1064535>
- Xu, X.-P., Kim, E., Swift, M., Smith, J. W., Volkmann, N., & Hanein, D. (2016). Three-dimensional structures of full-length, membrane-embedded human  $\alpha (11\beta) \beta 3$  integrin complexes. *Biophysical Journal*, 110(4), 798–809. <https://doi.org/10.1016/j.bpj.2016.01.016>
- Zheng, W. (2008). A unification of the elastic network model and the gaussian network model for optimal description of protein conformational motions and fluctuations. *Biophysical Journal*, 94(10), 3853–3857. <https://doi.org/10.1529/biophysj.107.125831>
- Zhou, D., Thinn, A. M. M., Zhao, Y., Wang, Z., & Zhu, J. (2018). Structure of an extended  $\beta 3$  integrin. *Blood*, 132(9), 962–972. <https://doi.org/10.1182/blood-2018-01-829572>

## SUPPORTING INFORMATION

Additional supporting information can be found online in the Supporting Information section at the end of this article.

**How to cite this article:** Joshi, O., Skóra, T., Yarema, A., Rabbitt, R. D., & Bidone, T. C. (2024). Contributions of the individual domains of  $\alpha 11\beta 3$  integrin to its extension: Insights from multiscale modeling. *Cytoskeleton*, 1–16. <https://doi.org/10.1002/cm.21865>